

This work was written as part of one of the author's official duties as an Employee of the United States Government and is therefore a work of the United States Government. In accordance with 17 U.S.C. 105, no copyright protection is available for such works under U.S. Law.

Public Domain Mark 1.0

<https://creativecommons.org/publicdomain/mark/1.0/>

Access to this work was provided by the University of Maryland, Baltimore County (UMBC) ScholarWorks@UMBC digital repository on the Maryland Shared Open Access (MD-SOAR) platform.

Please provide feedback

Please support the ScholarWorks@UMBC repository by emailing scholarworks-group@umbc.edu and telling us what having access to this work means to you and why it's important to you. Thank you.

JGR Space Physics



METHOD

10.1029/2021JA029637

Key Points:

- A novel method for capturing the energy dispersion structure is developed and applied to the DMSP data
- The algorithm is applied and validated against a G2-class Moderate Storm
- New types of ion dispersion events are uncovered with the algorithm and their relevance is stated

Correspondence to:

D. da Silva,
daniel.e.dasilva@nasa.gov

Citation:

da Silva, D., Chen, L. J., Fuselier, S., Wang, S., Elkington, S., Dorelli, J., et al. (2022). Automatic identification and new observations of ion energy dispersion events in the cusp ionosphere. *Journal of Geophysical Research: Space Physics*, 127, e2021JA029637. <https://doi.org/10.1029/2021JA029637>

Received 4 JUN 2021

Accepted 24 MAR 2022

Author Contributions:

Conceptualization: D. da Silva, L. J. Chen

Data curation: D. da Silva

Formal analysis: D. da Silva

Funding acquisition: L. J. Chen

Investigation: D. da Silva, B. Burkholder

Methodology: D. da Silva, L. J. Chen, S. Wang

Software: D. da Silva

Supervision: L. J. Chen

Validation: D. da Silva, L. J. Chen

Visualization: D. da Silva








Writing – original draft: D. da Silva

Writing – review & editing: D. da Silva, L. J. Chen

©2022. The Authors.

This is an open access article under the terms of the [Creative Commons Attribution License](https://creativecommons.org/licenses/by/4.0/), which permits use, distribution and reproduction in any medium, provided the original work is properly cited.

Automatic Identification and New Observations of Ion Energy Dispersion Events in the Cusp Ionosphere

D. da Silva^{1,2,3} , L. J. Chen¹ , S. Fuselier⁴ , S. Wang^{1,5} , S. Elkington² , J. Dorelli¹ , B. Burkholder^{1,3}, and D. Sibeck¹ 

¹NASA Goddard Spaceflight Center, Heliophysics Sciences Division, Greenbelt, MD, USA, ²Laboratory for Atmospheric and Space Physics, University of Colorado, Boulder, CO, USA, ³Goddard Planetary Heliophysics Institute, University of Maryland, Baltimore County, Baltimore, MD, USA, ⁴Southwest Research Institute, San Antonio, TX, USA, ⁵Department of Astronomy, Goddard Planetary Heliophysics Institute, University of Maryland, College Park, MD, USA

Abstract In this paper we present an algorithm which identifies ion energy dispersion events in low altitude cusp observations. Such an algorithm is suitable for implementation to prioritize data for downlink, or to be run on the ground for data mining. The energy dispersion events, sometimes known as dispersed particle precipitation, have been interpreted as due to time-of-flight effects of energized ions from magnetopause reconnection sites. Our algorithm utilizes a novel method of integrating a scoring function across moving time windows to capture the dispersion structure. The algorithm is implemented and prototyped with Defense Meteorological Satellite Program data but specified in terms that apply to other missions for both ions and electrons. Two new types of dispersion events are uncovered with the algorithm, consisting of a cold inverse double dispersion event where one population dominates, and a V-type dispersion event during northward interplanetary magnetic field.

Plain Language Summary Ion energy dispersion events occur in the low altitude cusp region, originating from reconnection at the magnetopause. This paper presents an algorithm for automatically detecting these events in data from the Defense Meteorological Satellite Program (DMSP) satellites. Though the algorithm is demonstrated with DMSP, the algorithm can work with other satellites. The algorithm is also used to search for new types of dispersion, and two new types of dispersion events are presented in this paper.

1. Introduction

Cusp ion energy-latitude dispersion events originate from dayside magnetopause reconnection and differences in parallel velocities of magnetosheath-origin ions that are accelerated in reconnection (Lockwood & Smith, 1989). When ions precipitate down the cusp field lines, the distribution of parallel velocities is translated into differences in time-of-flight over the path to the ionosphere. Meanwhile, during a southward interplanetary magnetic field (IMF), reconnected magnetic field lines convect toward higher-magnetic latitudes (MLAT). The result is that upon arrival, the injected ions become organized by their parallel velocity across a span of MLAT, with the energy decreasing with increasing MLAT for southward IMF. Analogously, during northward IMF, the ion energy increases with increasing MLAT. The MLAT-dependent ion energies—correlated with their parallel velocities after reconnection acceleration—are the final form of the dispersion.

Satellites like Defense Meteorological Satellite Program (DMSP) which measure the particle fluxes as a function of energies in the ionosphere capture dispersion structures in ion energy spectrograms. An example of an event in the DMSP data (Figure 1) shows the ion energies decreasing with time. With DMSP, the time axis corresponds approximately to the magnetic latitude. The satellite traveling at a speed of 7.8 km/s passes through the event entirely in under 60 s.

Ion dispersion events have been linked to fundamental reconnection variables, such as the reconnection rate (Lockwood & Smith, 1992; Trattner et al., 2005), and the direction of the interplanetary magnetic field (Connor et al., 2015; Onsager et al., 1995; Wing et al., 2001). Other than DMSP, missions that have studied the ion dispersion structures include Cluster (Escoubet et al., 1997), Polar (Harten & Clark, 1995), Fast Auroral Snapshot (Carlson et al., 1998), and TRICE-2 (Kletzing et al., 2019; Sawyer et al., 2021).

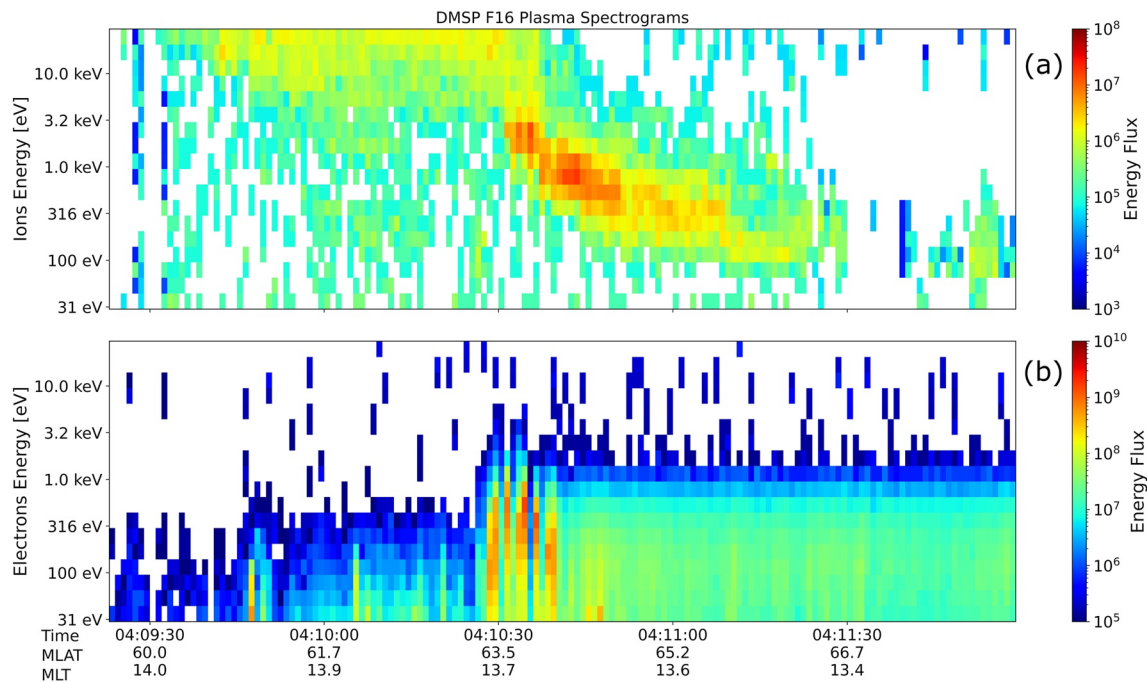


Figure 1. An example of an ion energy-latitude dispersion event from Defense Meteorological Satellite Program. The key feature to observe is the change in the ion spectrogram energies over the course of the event (Panel (a)) and the concurrent electron energy flux showing high fluxes below 1 keV, characteristics of magnetosheath (Panel (b)).

As of 2021, the DMSP mission has a four-decade coverage of measuring precipitating plasmas in the cusp ionosphere, the longest-running record of all missions. Flying at altitudes between 840 and 860 km, the DMSP constellation is composed of multiple satellites in sun-synchronous orbits carrying top-side facing electron and ion instruments with a 90° FOV (Redmon et al., 2017). These instruments are jointly called the Special Sensor J (SSJ) instruments. The SSJ from the DMSP generation used for this study (which is SSJ/5, the fifth Generation), provides ion and electron spectrogram data in 16 log-spaced energies between 30 eV and 30 keV, designed to match the previous generation known as SSJ/4 (Hardy, 1984). The instruments are composed of triquadrascopic electrostatic analyzers (ESAs) which cover six non-overlapping look directions (Redmon et al., 2017). For this work, we use the ion and differential energy flux data in the released units of 1/(cm²*s*sr). Should the method be adapted to a different satellite mission, equivalent measurements may require normalization to be in units independent of the size of the energy bins. We note that while SSJ/5 was designed with angular information, the standard operating configuration was revised to sum over these look directions to reduce telemetry (Redmon et al., 2017). While this is acknowledged, it does not impact this method as only non-directional spectrogram data is used.

This paper presents an algorithm developed to detect ion dispersion events automatically. The benefit of having an effective algorithm to detect events is both operational and scientific. In the operational consideration, the algorithm can be used to prioritize events for data downlink. Scientifically, the algorithm can be used for data mining, as a low-effort way to search for ion dispersion events and enable statistics.

The algorithm draws heavily from the heritage of Lockwood and Smith (1992). These authors introduced a key variable to characterize the dispersion structure: the lower cutoff energy (E_{ic}) of the ion spectrogram. Because low-energy ions crossing the magnetopause and injected onto newly opened field lines may not yet have arrived at the ionosphere by the time the satellite flies through the cusp, there is a minimum cut-off energy for ions observed. Lockwood and Smith define the cut-off as the energy whose flux is 10% of the peak flux across all energies at a given time. The authors state that the choice of 10% is semi-arbitrary, but alternate definitions do not significantly alter the results obtained. For this paper, we utilize their definition for the purpose of convention within the literature.

E_{ic} simplifies the energy spread into a scalar quantity that can be tracked for changes. A quasi-steady change in this variable is indicative of the dispersion structure of the event: change in energy across MLAT. Looking for dayside events with changes in E_{ic} concurrent with an electron population at magnetosheath energies during southward IMF leads to the base form of the algorithm presented in this paper. The algorithm can be readily adjusted to search for dispersion events during northward IMF or non-standard dispersion as will be discussed later.

In the *Methods* section, we formulate all the required changes in E_{ic} and the associated conditions into a rigorous definition translatable to computer code. After the methodology is established, it is applied to a storm to demonstrate the power of the event finding capability. This can be found in the section titled *Application to the 20 December 2015 Storm*. A detailed investigation into the performance of the technique compared against a set of hand-picked events can be found in the *Calibration and Validation* section. In the *New Science Events* section, we present new and unusual observations of cusp phenomena found by the algorithm and discuss how the base form of the algorithm was adapted to find them.

2. Methods

The algorithm is based on a sliding window approach. It walks through time with a sliding window of fixed length and computes an instantaneous score $D(t)$ at each time step. The algorithm uses this score to decide whether the window has an event. When multiple overlapping windows have events, they are merged. The score can be negative, if the data at that time step is so strongly against the notion of it constituting an event that the window should not be selected.

The primary condition for deciding a window has an event is whether the total score $\int D(t)dt$ is above a threshold. A minor condition is that the ratio of the integral of $D(t)$ to the integral of $|D(t)|$ is 80%. The minor condition was found in practice to be effective. The threshold for accepting a window based on a total score is a sensitivity, which can be adjusted to make the algorithm accept more or fewer events depending on the goals.

The scoring function is the core of the algorithm. $D(t)$ is a function of the ion and electron spectrograms and upstream IMF conditions. In our prototype, these data come from DMSP and OMNI.

Within $D(t)$, the most important term is the rate of change of the log-scale scalar energy, denoted as $d\text{Log}(E_{ic})/dt$. Following Lockwood and Smith (1992), E_{ic} is defined as the energy at which the flux is 10% of the peak flux over energy at a given time.

The algorithm finds the value of E_{ic} by looking for the energy of the peak flux, and then stepping the energy channel downwards until it finds where the flux gets to the 10% level. In a bimodal flux distribution where two flux peaks are present, this method selects the population with the peak flux.

The calculation of $d\text{Log}(E_{ic})/dt$ must be done with care. In the ion case the first two energies (30 and 44 eV) are skipped due to noise issues. This is done only to avoid a DMSP noise issue and may not be necessary in adaptations to other satellite missions which have reduced or eliminated noise in those channels. The derivative $d\text{Log}(E_{ic})/dt$ uses a smoothed version of $\text{Log}(E_{ic})$ over time which was found in practice to be effective in removing false positives. The spectrogram is not itself smoothed. The smoothing of $\text{Log}(E_{ic})$ is done with a moving average using a window size of 11 data points. This smoothing helps the algorithm become more well-behaved in the face of noise and abrupt changes.

Equation 1—Classification Function

$$\text{Accept if } \int_{\text{window}} D(t) dt > \tau \text{ and } \frac{\int D(t) dt}{\int |D(t)| dt} > 0.8 \quad (1)$$

$$\text{where: } D(t) = -\text{sgn}\left(\frac{d|\text{MLAT}|}{dt}\right) \left[\frac{d[\text{Log} E_{ic}]_{\text{smoothed}}}{dt} \right] a_i(t) a_e(t) b(t) c(t) d(t) e(t)$$

$$a_i(t) = \begin{cases} 1 & \text{if average ion differential energy flux between 65 eV and 3.2 keV} > 10^5 \text{ 1/(cm}^2 * \text{s * sr)} \\ 0 & \text{otherwise} \end{cases}$$

$$\begin{aligned}
 a_e(t) &= \begin{cases} 1 & \text{if average electron differential energy flux under } 3.2 \text{ keV} > 10^6 \text{ } 1/(\text{cm}^2 * s * sr) \\ 0 & \text{otherwise} \end{cases} \\
 b(t) &= \begin{cases} 1 & \text{if IMF } B_z < -3 \text{ nT} \\ 0 & \text{otherwise} \end{cases} \\
 c(t) &= \begin{cases} 1 & \text{if ion flux at } E_{ic} \text{ is greater than } 10^5 \text{ } 1/(\text{cm}^2 * s * sr) \\ 0 & \text{otherwise} \end{cases} \\
 d(t) &= \begin{cases} 1 & \text{if } E_{ic} \text{ is less than } 3.2 \text{ keV (energy threshold for accelerated ions of magnetosheath origin)} \\ 0 & \text{otherwise} \end{cases} \\
 e(t) &= \begin{cases} 1 & \text{if } 6 < \text{MLT} < 18 \text{ and } |\text{MLAT}| > 55^\circ \\ 0 & \text{otherwise} \end{cases}
 \end{aligned}$$

Equation 2—Moving Average Smoothing

$$[\text{Log } E_{ic}]_{\text{smoothed}}(t_i) = \frac{1}{11} \sum_{\Delta i=-5}^{\Delta i=+5} [\text{Log } E_{ic}](t_{i+\Delta i}) \quad (2)$$

The variable τ represents an adjustable threshold which can be used to tune the algorithm (see Calibration and Validation). τ corresponds to units of net change of E_{ic} in units $\Delta \text{Log}(eV)$ wherein changes only contribute to the net change when they occur under certain conditions outlined in the additional terms. These additional terms such as $a_i(t)$ are included in $D(t)$ to zero out the score when certain conditions are not met. The $a_i(t)$ and $a_e(t)$ terms set the score to zero when the average fluxes (ion and electron respectively) over lower energies is too low. The energy range used for the average is 30 eV to 3.2 keV for electrons and 65 eV to 3.2 keV for ions. In the case of ions, the 30–65 eV energies were excluded to avoid noise issues. Overall, the averaging is done to ensure that the selected events meet the magnetosheath high energy flux criteria. The $b(t)$ term sets the score to zero if the southward IMF B_z is too weak, as we focus our test of the algorithm to strongly southward IMF (effects of varying B_z strength are discussed in the *Calibration and Validation* and *New Science Events* sections). The $c(t)$ term sets the score to zero if the ion flux at E_{ic} is not large enough, serving as a supporting companion to the flux requirement in $a_i(t)$ to enable sufficient counting statistics. The $d(t)$ term sets the score to zero when E_{ic} is too high to be considered related to the magnetosheath. Finally, the $e(t)$ term sets the score to zero on the night-side or at MLAT outside the cusp.

The $-sgn\left(\frac{d|\text{MLAT}|}{dt}\right)$ term ensures that the selected events have decreasing E_{ic} with increasing MLAT, as expected for dayside magnetopause reconnection under southward IMF. Because we differentiate $\text{Log}(E_{ic})$ with respect to time and not magnetic latitude, this term works to counteract the loss of information about the direction the satellite is moving, adding back whether the energies should increase or decrease with time. Together $-sgn\left(\frac{d|\text{MLAT}|}{dt}\right)$ and $\left[\frac{d\text{Log}(E_{ic})}{dt}\right]$ complement each other to keep the score positive only when the energy change is in the intended direction.

The algorithm can be adapted for studies of events with reverse dispersion by dropping the leading minus sign of the $-sgn\left(\frac{d|\text{MLAT}|}{dt}\right)$ term. Under circumstances such as northward IMF, ion dispersion events with slopes opposite to those during southward IMF occur in nature. Past studies suggest a relationship between the dispersion slope and the IMF clock angle, wherein northward and southward IMF produce energy-latitude dispersion in opposite directions (Connor et al., 2015; Onsager et al., 1995; Wing et al., 2001).

It is worth noting that DMSP satellites are in near-polar, sun-synchronous orbits with an inclination of about 98.8° (Burke et al., 2011) and local time of descending nodes varying between spacecraft (F16 - 7:54, F17 - 5:35, F18 - 8:00). Because of the near-polar orbit, we approximate the change of E_{ic} over magnetic latitude (proxy for change of E_{ic} along the magnetic field convection direction, assuming that the magnetic field convection is mainly across the MLAT) by $d(E_{ic})/dt$. A non-polar orbit will still work with this algorithm, but one should reduce the integral threshold from this study to suit the different rate the satellite traverses magnetic latitude.

Multiple use cases can be applied to automatic event identification. For some use cases, users may want only very clean events with few false positives. In other cases, users may be interested in catching a wider net of events, and willing to remove false positives by hand. The algorithm can cover this spectrum of use cases by adjusting the threshold associated with the integral to change the algorithm's sensitivity.

The concept behind the sliding window approach is that if we can find a function of instantaneous score, we can integrate over a window to determine if that window contains an event. In our case, the good notion of an instantaneous score comes from the change in the scalar energy variable E_{ic} , with some other terms multiplied to set the score to zero. The change in E_{ic} is the most important information and is the heart of the algorithm, with the additional terms included to add in a-priori knowledge and help the process.

3. Application to the 20 December 2015 Storm

The algorithm is applied to the 20 December 2015 storm with the search including two days before and after (the 18th to the 23rd). The minimum Dst is -170 nT. The storm was classified by NOAA as type G2 (Moderate), according to the NOAA geomagnetic storm scale. Storms of this severity occur approximately 600 times (on 360 days) per solar cycle and correspond to $K_p = 6$ (NOAA Space Weather Scales, 2021).

Two example ion dispersion events detected from the 20 December 2015 storm are shown in Figure 2. In these plots, the panels are (a) the ion spectrogram, with E_{ic} as the blue line and the energy threshold as a dotted black line (b) the electron spectrogram and (c) the instantaneous score $D(t)$. Note how the instantaneous $D(t)$ scoring function contributes positively when the ion peak-flux energy varies with magnetic latitude (time), a magnetosheath electron population is present, and the bulk of the ion population is under the threshold energy.

4. Calibration and Validation

The method is calibrated and validated using techniques emerging in the literature of algorithmic space physics and data science. The goal of this calibration/validation is to both test the effectiveness of the algorithm against hand-picked results, and to optimize/understand the sensitivity to the adjustable parameters and miscellaneous tolerances which appear in Equation 1.

The algorithm is tested against a set of hand-picked events from the 20 December 2015 storm. Hand-picked data originated from a search between December 18 and December 22 (5 days total), searching in 5-min increments at a time. This was done for the F16, F17, F18, and F19 DMSP satellites. In total, 16 events were found.

To discuss the calibration and validation statistically, it is useful to formalize the decision process used by the algorithm. At the heart, this automatic identification algorithm is a binary classifier characterized by the following components:

1. A classification function $C(\bar{X}; \bar{\theta})$ whose input is an interval of data condensed into data vector \bar{X} , whose output is a total scalar score rating the occurrence of an event in the interval, and whose tunable options are condensed into $\bar{\theta}$.
2. A classification threshold τ wherein it is agreed that if the total score is above the threshold, it is decided that an event occurs in the interval (and if under the threshold, it does not).

This is summarized in Equation 3, where the interval of data corresponds to vector \bar{X} , the tunable options to vector $\bar{\theta}$, the classification threshold to τ , and the classification function $C(\bar{X}, \bar{\theta})$ corresponding to the integrated instantaneous score $D(t)$ over the window.

Equation 3

$$\text{EventExists}(\bar{X}; \bar{\theta}) = \begin{cases} \text{true} & \text{if } C(\bar{X}; \bar{\theta}) \geq \tau \\ \text{false} & \text{if } C(\bar{X}; \bar{\theta}) < \tau \end{cases} \quad (3)$$

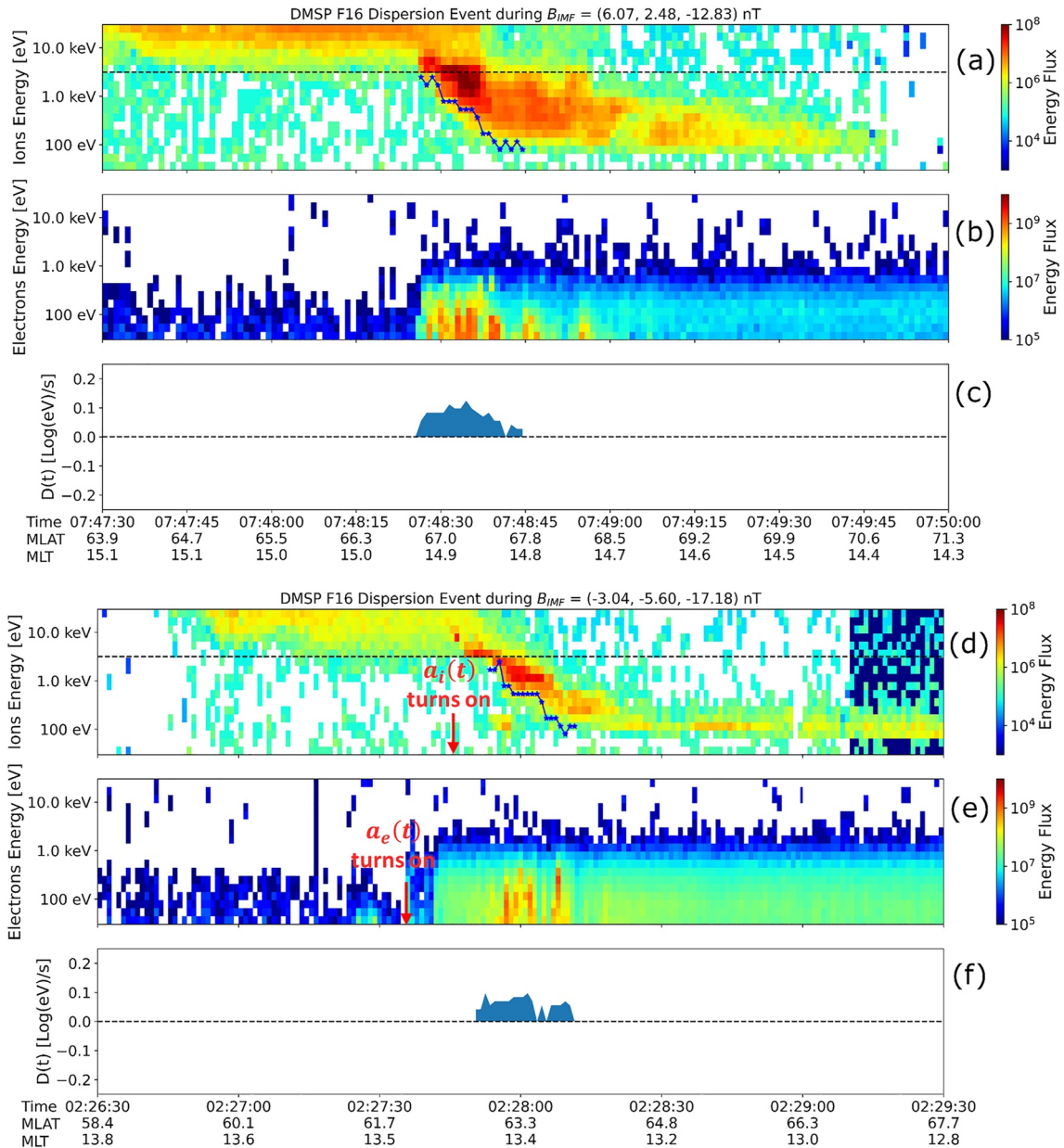


Figure 2. Two of the 25 events detected by the algorithm from the 20 December 2015 G2 moderate geomagnetic storm. The dates of the search were December 18th to 23rd. In these plots, the panels are (a)/(d) ion spectrogram with E_{ic} as the blue line and the energy threshold as a dotted black line (b)/(e) the electron spectrogram and (c)/(f) the instantaneous score $D(t)$. The blue line is the E_{ic} parameter. The curve plotted in panels (c)/(f) is the scoring function $D(t)$, with the area under the curve shaded to highlight the integral quantity. The area under $D(t)$ over an interval is compared against a threshold to determine whether the interval contains an event (see Equation 1). The arrows in the bottom plot indicate the points in time where $a_i(t)$ and $a_e(t)$ (average flux threshold for ions and electrons respectively) turn on, to illustrate when threshold values are met.

Adjustment of the threshold slides the trade-off in two variables known as the true positive ratio (TPR) and the false positive ratio (FPR). The TPR is defined as number of valid detections divided by total number of hand-picked events, sometimes called sensitivity. The FPR is defined as the number of false detections divided by the total number of intervals not containing a hand-picked event. This methodology has been pioneered in space physics literature by Comporeale et al. (2017) (classifying solar wind), dos Santos et al. (2020) (identifying flux rope signatures), and Argall et al. (2020) (identifying magnetopause crossings). A discussion of statistical validation in this nature from a data science perspective can be found in Hastie et al. (2009).

Table 1
Trade-Off Between the True Positive Ratio (TPR) and False Positive Ratio (FPR) as the Classification Threshold (τ) Is Varied

Threshold (τ)	True positive ratio (TPR)	False positive ratio (FPR)
0.1	1.00	0.100
0.2	1.00	0.064
0.3	1.00	0.051
0.4	1.00	0.039
0.5	0.94	0.028
0.6	0.88	0.020
0.7	0.81	0.015
0.8	0.69	0.011
0.9	0.56	0.008
1.0	0.52	0.006

Note. The TPR is defined as number of valid detections divided by total number of hand-picked events, sometimes called sensitivity. The FPR is defined as the number of false detections divided by the total number of intervals not containing a hand-picked event.

Different applications may call for a different prioritization of a good true positive ratio versus a good false positive ratio. For instance, selection of events for a statistical study may prefer lower false detections at the cost of missing some events (good FPR over good TPR), while implementation on-board a spacecraft may prefer selecting all the real events at the expense of false detections (good TPR over good FPR). Overall, the skill associated with a classification algorithm is how well it can afford a high true positive ratio while keeping the false positive ratio low.

The calibration studies the performance of the algorithm with multiple sets of tunable options and thresholds. The tunable options varied were the sliding window size (between 15 and 120 s in increments of 15 s), the minimum B_z -south strength (between -1 nT and -5 nT in increments of 1 nT), and the threshold τ (between 0.1 and 1.0 in increments of 0.1). It should be noted that $C(\bar{X}; \bar{\theta})$ does not necessarily need to be between 0 and 1 by any mathematical constraint, but rather coincidentally falls in this range.

The study finds that the most effective window size was 60 s, and the most effective minimum B_z -south strength was -3 nT. When the window size is under 60 s, performance degraded slightly, and when the window size is greater than 60 s no improvement is found. This is understood to be because the window must be sufficiently large to capture the full dispersion structure and decline in E_{ic} .

When the required B_z -south strength is relaxed from -3 nT to -2 nT and -1 nT, no further benefit is found. When the strength is increased to -4 nT and -5 nT, hand-picked events stopped being detected. It is possible that different conditions may produce events requiring a more relaxed B_z -south strength; users of the algorithms should take considerations with setting this parameter.

A table of the trade-off between the true positive ratio and the false positive ratio using these optimal tunable parameters is found below. It is considered a success when the threshold is sufficiently low, 100% of the events from the hand-picked set were detected with a false positive ratio of about 4%. This occurs at a threshold of $\tau = 0.4$, which we consider a reasonable balance for most applications. In a use case like implementation on-board a spacecraft to filter unnecessary downlink, this indicates that under conditions similar to the 20 December 2015 storm, one would be able to reduce the data downlink by 96% while still transmitting all the events of interest (Table 1).

5. New Science Events

After applying the algorithm to search for standard dispersion events, we discuss its applications to find non-standard dispersion in this section. Standard events are characterized as occurring during B_z -south (B_z -north) where the energy-dispersion relation requires increasing energy at decreasing (increasing) MLAT. However, other forms of dispersion exist. For example, overlapping dispersion events wherein multiple cusp ion injections overlap in space and time (Fuselier et al., 1997; Lockwood, 1995; Pitout et al., 2012). In this section we present observations of the new types of events found using the algorithm and state their scientific relevance. In each case, we discuss which modifications were required to tailor to each class of event.

6. Cold Inverse Double Dispersion

A new observation of an inverse double dispersion where two ion populations with energy-MLAT dispersion overlap in time and the dispersion direction is opposite to that prescribed by the field line convection direction is presented in Figure 3. The time of the event is 29 August 2015, at 9:07:20 UTC. This event is notable because the two observed dispersions almost overlap entirely (start/end at approximately the same time) and are relatively cold, significantly colder than those reported by Pitout et al. (2012). Furthermore, the direction of the dispersion is opposite of that which would be expected during an IMF with a southward B_z component (to be discussed in

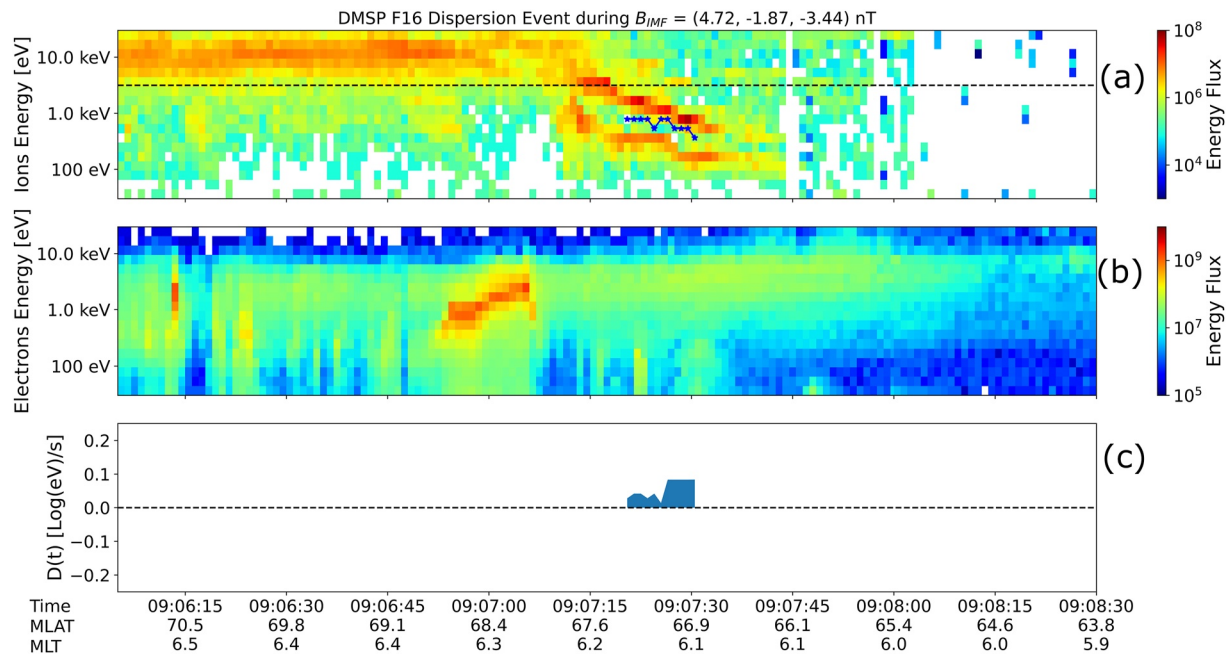


Figure 3. Cold Inverse Double Dispersion event selected by the algorithm. This event occurs on 29 August 2015, at 9:07:10–09:07:35 UTC. This event is notable because of the multiple dispersed populations observed at the same time. Modifications to the algorithm were made to find this event.

following paragraphs). Based on available OMNI data, the IMF during the event has a southward B_z and a dominant B_x , a condition conducive to generation of foreshock magnetic structures with earth-sized regions of strong B_{yz} (Chen, Wang, et al., 2021) that have been shown to induce magnetopause reconnection beyond the standard scenario (Chen, Ng, et al., 2021). Reconstruction of the IMF at the bow shock nose based on the highest available cadence data from the upstream monitors Wind and ACE spacecraft (Burkholder et al., 2020) indicate that B_z stays negative for at least 10 min before and after the selected double dispersion event. Nonetheless, the observed dispersion has E_{ic} has an E_{ic} curve which increases with MLAT. This event occurs at magnetic local times of ~ 6.1 – 6.2 . Whether the observed double dispersion presents a non-standard magnetopause reconnection scenario will require future research to solidify the IMF condition. Nonetheless, the new observation will stimulate new investigations on solar wind-magnetosphere-ionosphere coupling.

To find this event, the algorithm was modified to search for dispersion wherein the energy increases (decreases) with increasing (decreasing) MLAT during an IMF with a negative B_z component. When encountering double dispersion and (multi-modal distributions in general) the algorithm places the E_{ic} energy relative to the population with the highest peak energy flux. By preferring the coinciding population with highest peak flux, the same detection logic remains applicable to the dispersion structure and the event becomes detectable. Despite the electron population at several keV, this event meets the magnetosheath electron criterion set by $a_e(t)$ as the averaged electron flux below 3.2 keV is above the threshold. We note that in double dispersion events where the peak flux switches between the two populations intermittently, using a single E_{ic} becomes insufficient to capture the dispersion structure and a multi- E_{ic} approach may be required.

In the standard picture, the northward or southward component of the IMF sets the direction of the field line convection during reconnection. For southward IMF reconnection, the field line moves tailward, and during northward IMF convection the field line moves toward the dayside. In standard dispersion, the field line convection direction combined with the time-of-flight effects prescribes how the dispersion manifests (Lockwood & Smith, 1989; Trattner et al., 2005). During southward IMF the standard dispersion has the characteristic energy increase (decrease) with decreasing (increasing) MLAT. During a northward IMF, standard dispersion dictates that the energy will increase (decrease) with increasing (decreasing) MLAT. This is summarized in Table 2.

The presented double dispersion event is unique as a scenario not found in this table. We call this *inverse dispersion*, wherein the direction is opposite of that prescribed by the time-of-flight effects and the field line convection direc-

Table 2

Standard Dispersion Direction Over Satellite Track From Traditional Reconnection Model

	Northward IMF	Southward IMF
Satellite moves toward increasing MLAT	E_{ic} increases with time	E_{ic} decreases with time
Satellites moves toward decreasing MLAT	E_{ic} decreases with time	E_{ic} increases with time

tion of standard dispersion. To search for this event, we modified the $D(t)$ instantaneous scoring function designed for standard dispersion during Southward IMF. In the standard southward IMF case, the $D(t)$ function multiplies the terms $-sgn\left(\frac{d|MLAT|}{dt}\right)$ and $\left[\frac{dLog(E_{ic})}{dt}\right]_{smoothed}$ so that the score is positive when E_{ic} is changing in the direction stated in the final column of Table 2. These multiplied terms yield a positive $D(t)$ when E_{ic} is changing in the proper direction for standard dispersion and a negative $D(t)$ when E_{ic} is changing in the wrong direction for standard dispersion. The modification to adapt $D(t)$ for inverse dispersion was to flip the minus sign, so in that (a) $D(t)$ becomes positive and contributes to a selection when E_{ic} changes in what was formerly the wrong direction, and (b) becomes negative and counts against a selection when E_{ic} changes in what is the proper direction for regular dispersion (Table 2). In this way, we look for a complementary set of dispersions outside the scenario of standard dispersion.

Equation 4—Standard Dispersion During Southward IMF Instantaneous Scoring Function (Restated)

$$D(t) = -sgn\left(\frac{d|MLAT|}{dt}\right) \left[\frac{dLog(E_{ic})}{dt}\right]_{smoothed} a_i(t)a_e(t)b(t)c(t)d(t)e(t) \quad (4)$$

$$\text{where: } b(t) = \begin{cases} 1 & \text{if IMF } B_z < -3 \text{ nT} \\ 0 & \text{otherwise} \end{cases}$$

Equation 5—Inverse Dispersion During Southward IMF Instantaneous Scoring Function

$$D(t) = +sgn\left(\frac{d|MLAT|}{dt}\right) \left[\frac{dLog(E_{ic})}{dt}\right]_{smoothed} a_i(t)a_e(t)c(t)b(t)d(t)e(t) \quad (5)$$

7. V-Type Dispersion

A notable selection that will potentially lead to new scientific understanding presents a V-type dispersion where E_{ic} first decreases and then increases with increasing MLAT. The IMF has a strong northward component and stable for 15 min before and after the event (based on OMNI). The increasing E_{ic} with increasing MLAT in the second part of the event is consistent with magnetopause reconnection occurring tailward of the cusp, expected when the IMF B_z is positive (Connor et al., 2015). However, the decreasing E_{ic} with increasing MLAT in the first part of the event is consistent with magnetic reconnection happening equatorward of the cusp, not expected for a positive IMF B_z , and hence is named inverse dispersion. An inverse dispersion displays an E_{ic} -MLAT slope opposite to that prescribed by the field line convection direction and time-of-flight effects. A similar observation with slightly lower energies and without a preceding electron signature is reported in Woch & Lundin, 1992. The dispersion event is found using a modified form of the algorithm, as indicated in Figure 4. During the V-type dispersion a high flux of electrons at magnetosheath energies occurs.

To adapt the algorithm to the northern IMF class of events, the function $D(t)$ was modified to search for inverse dispersion and the $b(t)$ term was replaced with a new term $b_p(t)$ (subscript p meaning “positive”) which enforces the requirement that $B_z > 0$ nT. The equations for the scoring functions in the standard model and this model are shown together in Equations 6 and 7 for comparison. The only differences are the sign flip to search for inverse dispersion and the replacement of $b(t)$ with $b_p(t)$.

Equation 6—Standard Dispersion Instantaneous Scoring Function (Restated)

$$D(t) = -sgn\left(\frac{d|MLAT|}{dt}\right) \left[\frac{dLog(E_{ic})}{dt}\right]_{smoothed} a_i(t)a_e(t)b(t)c(t)d(t)e(t) \quad (6)$$

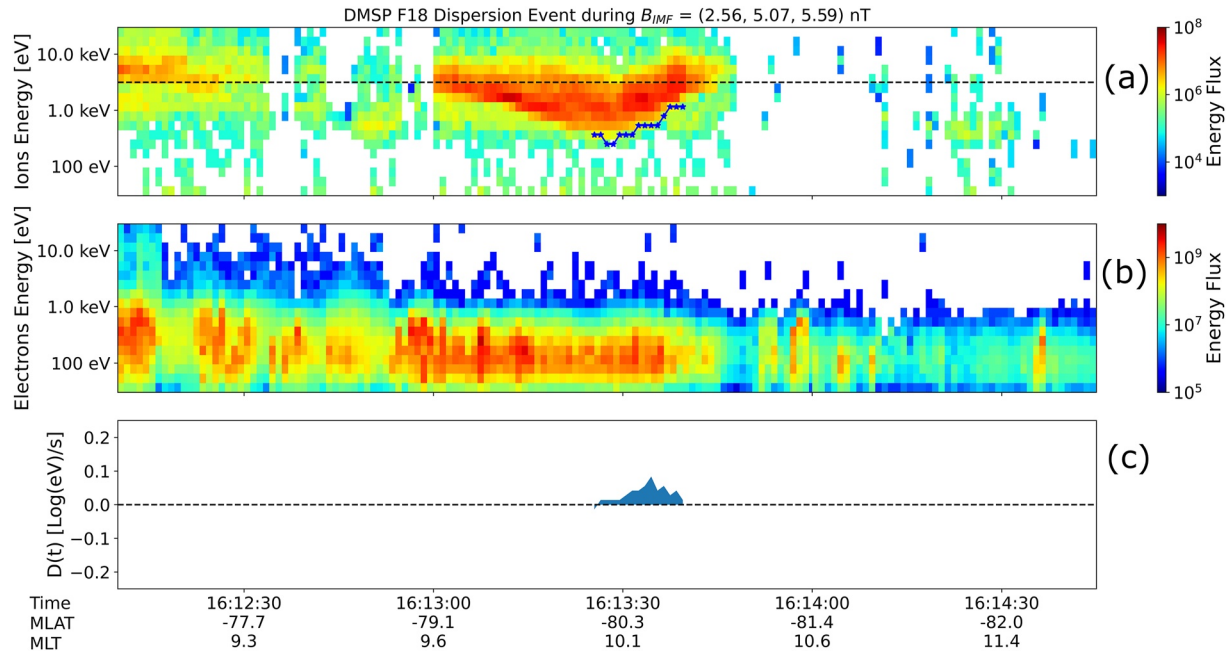


Figure 4. “V” Dispersion event during a stable northward IMF on 24 December 2015 at 6:13:00–06:13:40 UTC. During the V-type dispersion, E_{ic} first decreases then increases with increasing magnetic latitudes, and the high flux of electrons is at typical magnetosheath energies. The algorithm was modified to find this event.

$$\text{where: } b(t) = \begin{cases} 1 & \text{if IMF } B_z < -3 \text{ nT} \\ 0 & \text{otherwise} \end{cases}$$

Equation 7—Inverse Dispersion and Northward IMF Instantaneous Scoring Function

$$D(t) = +sgn\left(\frac{d|MLAT|}{dt}\right) \left[\frac{d\text{Log}(E_{ic})}{dt}\right]_{\text{smoothed}} a_i(t)a_e(t)c(t)b_p(t)d(t)e(t) \quad (7)$$

$$\text{where: } b_p(t) = \begin{cases} 1 & \text{if IMF } B_z > 0 \text{ nT} \\ 0 & \text{otherwise} \end{cases}$$

8. Summary

In this paper, we demonstrate the capability of an auto-detection algorithm to identify ion energy dispersion events in low altitude cusp observations. We show that the algorithm, in multiple modified forms, succeeds in finding two non-standard cusp ion energy-dispersions: cold inverse double dispersion dominated by one population (**Error! Reference source not found.**3) and V-type dispersion (Figure 4). For the both events, the algorithm was modified to look for dispersion in the inverse direction, and in the V-type case the algorithm was also modified to look for dispersion during IMF where $B_z > 0$.

These events illustrate the algorithm's potential for scientific yield in addition to the base model's flexibility to be adapted to new types of events. Because the algorithm is fully physics-based with a clean separation in terms between the energy/magnetic-latitude relationship and multiple true/false a priori assumptions, the algorithm can be modified based on physical understanding and scientist intuition. With this dissectible form, the algorithm holds strength in generalizability. In the *Conclusion* section, the power of the algorithm is reviewed and applications to science, operations, and on-board autonomy are discussed.

9. Conclusion and Outlook

In this paper, an algorithm to identify ion dispersion events is described and demonstrated with applications to the DMSP data. The algorithm's ability to find standard dispersion events in a geomagnetic storm is demonstrated, and the algorithm's performance is validated using statistical methodology established in space physics literature. The algorithm's scope to non-standard dispersion such as double dispersion and V-type dispersion is discussed, and the benefits of the physics-based approach are reviewed. New events of each of these non-standard types of dispersion are presented. Overall, the technical aspects of the algorithm are established and usages to further scientific and practical purposes are discussed.

Scientific usages of the algorithm include aggregating events in order to perform further scientific analysis on the events. Prime examples include for further investigations (a) analyzing the magnetopause and ionosphere reconnection rates inferred from the dispersion structure, using the methodology established in Equations 7 and 8 of Lockwood and Smith (1992) wherein the ion time-of-flight, tailward-bound field line geometry, and the E_{ic} calculation are used to estimate the reconnection rate (b) comparing the rate of storm-time event occurrence to the storm phase using metrics such as SYM-H and Dst.

Among practical usages include instrument operations centers for missions pushing the limits of data resolution that have implemented scientist-in-the-loop systems (Fuselier et al., 2016), sometimes called SITL or human-in-the-loop. These systems which use humans to rank time intervals of low-resolution data for priority transmission in their high-resolution form, are sometimes augmented by artificial intelligence suggestions (Argall et al., 2020). We suggest that a cusp mission pushing the limits of data rate consider this algorithm to augment a human decision, or even make the low-vs-high transmission decision onboard.

An avenue for future extension of the algorithm is adaptation to double dispersion, particularly in the case where one population does not dominate. This may be approached by detecting bimodal distributions which are not overlapping in energy, through a search for two local maxima via analysis of the first and second derivatives of the instantaneous differential energy flux versus energy curve. If such detection is successfully applied and the two populations can be sufficiently separated, a separate E_{ic}^{top} and E_{ic}^{bottom} could be calculated and the current method applied twice. A related and more challenging problem is the detection of bimodal distributions which overlap in energy, wherein the two signals must in some way be deconvolved.

In conclusion, our work opens a territory of algorithm development that puts hard definitions on the criteria for observed phenomena. These hard definitions become models themselves for understanding the phenomena. Furthermore, the hard definitions can be executed by a computer, allowing practical benefits for operations and science.

Data Availability Statement

The data used in this publication is publicly available from the CEDAR Madrigal Database (<http://cedar.open-madrigal.org/>) and the Space Physics Data Facility (https://spdf.gsfc.nasa.gov/pub/data/omni/omni_cdaweb/hro_1min).

References

- Argall, M. R., Small, C. R., Piatt, S., Breen, L., Petrik, M., Kokkonen, K., et al. (2020). MMS SITL Ground Loop: Automating the burst data selection process. *Frontiers in Astronomy and Space Sciences*, 7, 54. <https://doi.org/10.3389/fspas.2020.00054>
- Burke, W. J., Wilson, G. R., Lin, C. S., Rich, F. J., Wise, J. O., & Hagan, M. P. (2011). Estimating Dst indices and exospheric temperatures from equatorial magnetic fields measured by DMSP satellites. *Journal of Geophysical Research*, 116(A1), A01205. <https://doi.org/10.1029/2010ja015310>
- Burkholder, B. L., Nykyri, K., & Ma, X. (2020). Use of the L1 constellation as a multispacecraft solar wind monitor. *Journal of Geophysical Research: Space Physics*, 125(7), e2020JA027978. <https://doi.org/10.1029/2020ja027978>
- Camporeale, E., Carè, A., & Borovsky, J. E. (2017). Classification of solar wind with machine learning. *Journal of Geophysical Research: Space Physics*, 122(11), 10–910. <https://doi.org/10.1002/2017ja024383>
- Carlson, C. W., Pfaff, R. F., & Watzin, J. G. (1998). The fast auroral snapshot (FAST) mission. *Geophysical Research Letters*, 25(12), 2013–2016. <https://doi.org/10.1029/98gl01592>
- Chen, L.-J., Ng, J., Omelchenko, Y., & Wang, S. (2021). Magnetopause reconnection and indentations induced by foreshock turbulence. *Geophysical Research Letters*, 48(11), e2021GL093029. <https://doi.org/10.1029/2021gl093029>
- Chen, L.-J., Wang, S., Ng, J., Bessho, N., Tang, J. M., Fung, S. F., et al. (2021). Solitary magnetic structures at quasi-parallel collisionless shocks: Formation. *Geophysical Research Letters*, 48(1), e2020GL090800. <https://doi.org/10.1029/2020gl090800>

Acknowledgments

The authors thank Dr. Craig Kletzing and Dr. Karlheinz Trattner for discussions of the algorithm during the preparation of this manuscript.

- Connor, H. K., Raeder, J., Sibeck, D. G., & Trattner, K. J. (2015). Relation between cusp ion structures and dayside reconnection for four IMF clock angles: OpenGGCM-LTPT results. *Journal of Geophysical Research: Space Physics*, 120(6), 4890–4906. <https://doi.org/10.1002/2015ja021156>
- dos Santos, L. F. G., Narock, A., Nieves-Chinchilla, T., Nuñez, M., & Kirk, M. (2020). Identifying flux rope signatures using a deep neural network. *Solar Physics*, 295(10), 1–29.
- Escoubet, C. P., Schmidt, R., & Goldstein, M. L. (1997). Cluster-science and mission overview. *The Cluster and Phoenix Missions*, 11–32. https://doi.org/10.1007/978-94-011-5666-0_1
- Fuselier, S. A., Lewis, W. S., Schiff, C., Ergun, R., Burch, J. L., Petrinec, S. M., & Trattner, K. J. (2016). Magnetospheric multiscale science mission profile and operations. *Space Science Reviews*, 199(1), 77–103. https://doi.org/10.1007/978-94-024-0861-4_4
- Fuselier, S. A., Shelley, E. G., Peterson, W. K., Lennartsson, O. W., Collin, H. L., Drake, J. F., et al. (1997). Bifurcated cusp ion signatures: Evidence for re-reconnection? *Geophysical Research Letters*, 24(12), 1471–1474. <https://doi.org/10.1029/97gl01325>
- Hardy, D. A. (1984). Precipitating electron and ion detectors (SSJ/4) for the block 5D/flights 6–10 DMSP satellites: Calibration and data presentation. *Report AFGL-TR-84-0317*.
- Harten, R., & Clark, K. (1995). The design features of the GGS wind and polar spacecraft. *Space Science Reviews*, 71(1), 23–40. <https://doi.org/10.1007/bf00751324>
- Hastie, T., Tibshirani, R., & Friedman, J. (2009). *The elements of statistical learning* (p. 33).
- Kletzing, C., Fuselier, S. A., Bonnell, J. W., Labelle, J. W., Moen, J., Trattner, K. J., et al. (2019). *The twin rockets to investigate cusp electrodynamics 2 (TRICE-2) mission* (Vol. 2019). AGU Fall Meeting Abstracts.
- Lockwood, M. (1995). Overlapping cusp ion injections: An explanation invoking magnetopause reconnection. *Geophysical Research Letters*, 22(9), 1141–1144. <https://doi.org/10.1029/95gl00811>
- Lockwood, M., & Smith, M. F. (1989). Low-altitude signatures of the cusp and flux transfer events. *Geophysical Research Letters*, 16(8), 879–882. <https://doi.org/10.1029/gl016i008p00879>
- Lockwood, M., & Smith, M. F. (1992). The variation of reconnection rate at the dayside magnetopause and cusp ion precipitation. *Journal of Geophysical Research*, 97(A10), 14841–14847. <https://doi.org/10.1029/92ja01261>
- NOAA Space Weather Scales. (2021). Retrieved from https://www.swpc.noaa.gov/sites/default/files/images/NOAA_scales.pdf
- Onsager, T. G., Fuselier, S. A., Petrinec, S. M., Yeoman, T. K., Escoubet, C. P., & Reme, H. (1995). Low-altitude observations and modeling of quasi-steady magnetopause reconnection. *Journal of Geophysical Research*, 100(A7), 11831–11843. <https://doi.org/10.1029/94ja02702>
- Pitout, F., Escoubet, C. P., Taylor, M. G. G. T., Berchem, J., & Walsh, A. P. (2012). Overlapping ion structures in the mid-altitude cusp under northward IMF: Signature of dual lobe reconnection? *Annales geophysicae* (Vol. 30, No. 3). Copernicus GmbH. <https://doi.org/10.5194/angeo-30-489-2012>
- Redmon, R. J., Denig, W. F., Kilcommons, L. M., & Knipp, D. J. (2017). New DMSP database of precipitating auroral electrons and ions. *Journal of Geophysical Research: Space Physics*, 122(8), 9056–9067. <https://doi.org/10.1002/2016ja023339>
- Sawyer, R. P., Fuselier, S. A., Kletzing, C. A., Bonnell, J. W., Roglans, R., Bounds, S. R., et al. (2021). TRICE 2 observations of low-energy magnetospheric ions within the cusp. *Journal of Geophysical Research: Space Physics*, 126(9), e2021JA029382. <https://doi.org/10.1029/2021ja029382>
- Trattner, K. J., Fuselier, S. A., Petrinec, S. M., Yeoman, T. K., Mouikis, C., Kucharek, H., & Reme, H. (2005). Reconnection sites of spatial cusp structures. *Journal of Geophysical Research*, 110(A4), A04207. <https://doi.org/10.1029/2004ja010722>
- Wing, S., Newell, P. T., & Michael Ruohoniemi, J. (2001). Double cusp: Model prediction and observational verification. *Journal of Geophysical Research*, 106(A11), 25571–25593. <https://doi.org/10.1029/2000ja000402>
- Woch, J., & Lundin, R. (1992). Magnetosheath plasma precipitation in the polar cusp and its control by the interplanetary magnetic field. *Journal of Geophysical Research*, 97(A2), 1421–1430. <https://doi.org/10.1029/91ja02487>